

Neural-Quantum-States Impurity Solver for Quantum Embedding Problems

Zhanghao Zhouyin,¹ Tsung-Han Lee,² Ao Chen,^{3,4} Nicola Lanatà,^{5,3} and Hong Guo¹

¹*Department of Physics, McGill University, Montreal, Quebec, Canada H3A2T8*

²*Department of Physics, National Chung Cheng University, Chiayi 62102, Taiwan*

³*Center for Computational Quantum Physics, Flatiron Institute, New York, New York 10010, USA*

⁴*Division of Chemistry and Chemical Engineering,*

California Institute of Technology, Pasadena, California 91125, USA³

⁵*School of Physics and Astronomy, Rochester Institute of Technology, Rochester, New York 14623, USA*

(Dated: September 17, 2025)

Neural quantum states (NQS) have emerged as a promising approach to solve second-quantised Hamiltonians, because of their scalability and flexibility. In this work, we design and benchmark an NQS impurity solver for the quantum embedding methods, focusing on the ghost Gutzwiller Approximation (gGA) framework. We introduce a graph transformer-based NQS framework able to represent arbitrarily connected impurity orbitals and develop an error control mechanism to stabilise iterative updates throughout the quantum embedding loops. We validate the accuracy of our approach with benchmark gGA calculations of the Anderson Lattice Model, yielding results in excellent agreement with the exact diagonalisation impurity solver. Finally, our analysis of the computational budget reveals the method’s principal bottleneck to be the high-accuracy sampling of physical observables required by the embedding loop, rather than the NQS variational optimisation, directly highlighting the critical need for more efficient inference techniques.

1. Introduction

Materials with strong electronic correlations have been the subject of extensive investigation in physics and materials science for decades. Such systems exhibit a variety of electronic phases, including metallic, insulating, and superconducting states [1], and represent a versatile design space for technological applications in electronics, quantum computing, and sensing. Designing new correlated materials with targeted properties therefore depends on the ability to solve the many-body electronic Hamiltonian, a computationally demanding task [2].

Quantum embedding (QE) methods provide a robust framework for overcoming these challenges [3–5]. The common strategy underlying these methods is to describe each fragment of interacting orbitals through an effective model, where its complex environment is replaced by a simpler, entangled quantum bath, designed to approximate its influence [3, 6]. The link between this effective model and the original system is established through self-consistency conditions, and different embedding schemes are defined by their choice of which physical property to match [3]. Dynamic mean-field theory (DMFT) [7–14], for instance, uses frequency-dependent one-body Green’s functions, whereas density matrix embedding theory (DMET) [5, 15–19] typically uses one- and two-body density matrices. The recently developed gGA [20–26] is a powerful variational method that generalizes the standard Gutzwiller Approximation (GA) [27–34] by systematically extending its variational space with auxiliary “ghost” fermionic degrees of freedom. This approach yields results in remarkable agreement with DMFT but at a much lower computational cost, as it requires calculating only the ground state of a finite-size impurity model, whereas DMFT requires the full spectra from an impurity model that corresponds to an

finite bath. Successful applications of gGA include accurate modelling of the Anderson lattice systems [21], excitonic phenomena [20], non-equilibrium systems [35] and altermagnetic systems [36], along with extensions that achieve charge self-consistency with density functional theory (DFT) [22], demonstrating its versatility and practical utility in real-material contexts.

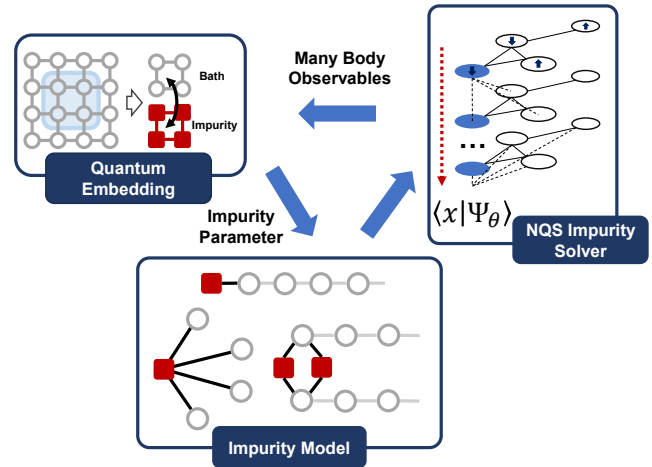


FIG. 1. The neural quantum states - quantum embedding (NQS-QE) workflow. The many-body Hamiltonian is embedded into impurity models via quantum embedding algorithms. It is then solved by the NQS impurity solver. The observables are derived from the graph neural network representation of the many-body wave function, which is then used to update the impurity parameters, thereby forming a self-consistent loop.

Despite the advances offered by QE methods, solving the impurity model remains a central computational bottleneck. Current impurity solvers include Exact Di-

agonalisation (ED) [37, 38], Numerical Renormalisation Group (NRG) [39, 40], Density Matrix Renormalisation Group (DMRG) [41, 42], and Quantum Monte Carlo (QMC) [43, 44]. While each of these methods has distinct advantages, their computational complexity often limits their application to practically relevant systems.

Neural Quantum States (NQS) [45–50], due to their inherent flexibility in representing wave functions in second-quantised formalisms, offer a compelling alternative to some of these challenges. In particular, their variational foundation provides us with controlled approximation errors through parameter optimisation [51]. Additionally, variational Monte Carlo provides us with a favourable computational scaling [52], especially advantageous for multi-orbital scenarios. The rapidly developing field of NQS shows promising trends toward a unified and scalable impurity solver [53, 54]. Nonetheless, impurity solvers based on NQS must address specific requirements, such as handling irregular hopping patterns and ensuring numerical stability and consistency. Accurately calculating observables from the optimised wave function further introduces additional methodological challenges.

In this work, we develop a graph transformer-based NQS impurity solver to represent arbitrarily connected impurity orbitals. We implement a systematic error control framework to rigorously bound uncertainties arising during the iterative optimisation and embedded properties sampling of the NQS wave function. Our model initialises node features with spin configurations and employs iterative graph attention mechanisms, achieving high flexibility in wave function representation. Optimisation efficiency is enhanced using recently proposed algorithms such as the Neural Network Pfaffian [55], MinSR[47] and SPRING[49]. Coupling our graph-based NQS solver with the gGA quantum embedding method, we validate its performance using benchmark Anderson Lattice Models [21], obtaining excellent agreement with ED solutions. Our results demonstrate the feasibility of employing NQS as impurity solvers within quantum embedding algorithms. Furthermore, we conduct extensive analyses of convergence behaviours across different error control parameters and computational timing, highlighting critical open questions that must be addressed to achieve scalable and practically relevant NQS-based impurity solvers.

The rest of the paper is organised as follows. In the next section, the technical details of the method are presented, including the NQS impurity solver, its associated error control, as well as its integration with the ghost Gutzwiller quantum embedding approach. In section 3, benchmark results associated with the Anderson Lattice Model and a detailed cost and error analysis of the NQS solver are illustrated. Finally, section 4 presents a discussion and a short summary of the NQS-gGA many-body formalism developed in this work.

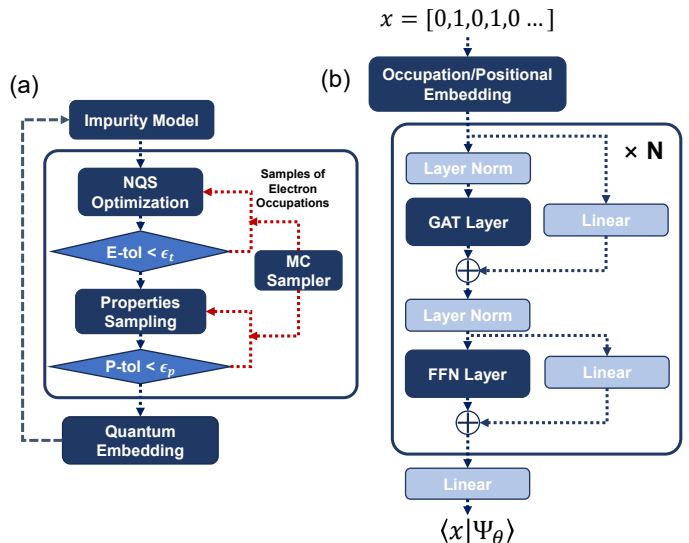


FIG. 2. (a) The workflow for the neural quantum states (NQS) impurity solver; The outer loop shows the impurity solver’s coupling with the quantum embedding method, which generates an impurity model for the NQS to solve. The solving process includes the NQS optimisation and properties sampling steps, with error control metrics E-tol and P-tol to guarantee convergence. The metrics are checked with tolerance ϵ_t and ϵ_p for energy and properties, respectively. Both steps are driven by the Monte Carlo (MC) sampler to compute expectations. (b) The neural network wave function’s architecture. The spin orbital configuration is first encoded with the occupation and positional embedding method, and passes through the main body of the network, which comprises N blocks of graph-transformer-like architecture with a residual connected graph attention (GAT) layer and a feed-forward neural network (FFN) layer.

2. The NQS-gGA formalism

In this section, we present the technical details of the NQS-gGA formalism developed in this work. As illustrated in Fig.2 (a), the impurity model, generated by the quantum embedding outer loops, will be fed into the NQS solving process, which consists of the NQS optimisation and properties sampling. For each step in the solving process, we have an error control metric to ensure the variance is minimised. In the following subsections, we will discuss the NQS method we used to construct the impurity solver in part A, the error control system that guarantees the stability of solving iterations in part B. In part C we will outline the gGA algorithmic structure.

A. Neural Quantum States Impurity Solver

The neural quantum state acts as a many-body wave function ansatz in the variational quantum Monte Carlo framework. Specifically, we consider an NQS wave func-

tion, expressed in second quantisation as follows:

$$|\Psi_\theta\rangle = \sum_x \langle x|\Psi_\theta\rangle|x\rangle = \sum_x \Psi_\theta(x)|x\rangle. \quad (1)$$

Here $|x\rangle$ are Fock states, where x encodes the corresponding spin-orbital occupation numbers, while Ψ_θ is a neural network, which takes an electronic configuration x as input and outputs the corresponding wave-function amplitude $\Psi_\theta(x)$.

Using NQS, the expectation of any operator \hat{O} is evaluated with Monte Carlo sampling as follows [56]:

$$\begin{aligned} \langle \hat{O} \rangle &= \mathbb{E}_{x \sim \Psi_\theta^2} [O_{loc}], \\ O_{loc} &= \frac{\langle x|\hat{O}|\Psi_\theta\rangle}{\langle x|\Psi_\theta\rangle}, \end{aligned} \quad (2)$$

where $\mathbb{E}_{x \sim \Psi_\theta^2}$ represents the expectation over the probability distribution of the current parameterized wave function Ψ_θ . We employ the Markov chain Monte Carlo [57] to perform sampling and the neighbour-exchange method [56] to generate new electron configurations. To approach the ground state, the NQS is optimised using stochastic reconfiguration [58] based on a recently proposed MinSR [47] and the SPRING [49] methods to stabilise and accelerate the calculation.

Impurity models can be constructed with distinct geometries, such as linear chains or star-like structures [59, 60], as shown in Fig. 1, which arise from different ways of representing the non-interacting bath. This flexibility requires a network architecture capable of handling arbitrary hopping patterns between orbitals. While transformer-based models effectively capture global interactions via attention mechanisms [61], their computational cost scales as $O(N^3)$, where N is the number of sites. Leveraging the sparse connectivity inherent to impurity models, we instead adopt the graph convolutional network ansatz. This reduces computation cost while maintaining the accuracy with an advanced network design.

More specifically, our graph-based model treats the orbital as graph nodes and single-particle interactions as edges. As illustrated in Fig.2 (b), we initialise the node message as the orbital occupation number vector, which is a binary vector of value 1/0. Then, the state vectors are passed into the occupation positional encoding layer, where four different occupations in one site ($|11\rangle, |01\rangle, |10\rangle, |00\rangle$) are mapped to different vector embeddings, as is commonly adopted in natural language processing [62]. Meanwhile, the positional information is added to the embedding vectors via the positional embeddings [62] to uniquely distinguish each orbital site, which results in our final embeddings with all necessary state information. Furthermore, the embeddings are passed through the main body of the model, backboneed by the GATv2 [63] graph attentional architecture. We mimic the transformer architecture by composing each iterative layer using one graph attention (GAT) layer and a feed-

forward neural network (FFN) layer with residual connections. After iterative accumulation, the features are then mapped via a linear layer to two real scalar quantities, corresponding to the wavefunction amplitude and the complex phases, as our wave function's output $\langle x|\Psi_\theta\rangle$

A significant challenge in building a stable solver is to define a clear error metric for the wave function optimisation. Conventional VMC provides an intuitive guideline — that lower variance typically correlates with reduced error, but the relationship is not quantitative. We will discuss this important issue in the following section.

B. Error Control System

A characteristic functional distinction between solving standalone Hamiltonians and acting as solvers to form self-consistent solutions is the requirement for numerical stability. In quantum embedding frameworks, the impurity model and the physical system are self-consistently coupled. The solution to the impurity model directly influences the state of the original system, which, in turn, affects the updates of the impurity problem itself. Uncontrolled errors can propagate through iterative loops, causing instability in the embedding procedure. Consequently, establishing a systematic error control methodology for the NQS solver within the variational Monte Carlo (VMC) framework is essential.

The errors arising in the VMC-NQS process can be categorised into two primary sources: (1) the wave function optimisation error; (2) the Monte Carlo sampling error. The wave function optimisation error refers to the discrepancy between the converged NQS wave function and the true ground-state wave function, which appears during the NQS optimisation steps in Fig.2 (a).

The quality of the optimised NQS wave function, $|\Psi_\theta\rangle$, is determined by how closely it approximates a true eigenstate of the impurity Hamiltonian. The most direct measure of this is the energy variance, $\text{Var}[E]$, which must vanish for an exact eigenstate and is therefore the fundamental diagnostic monitored during optimisation:

$$\begin{aligned} \text{Var}[E] &= \mathbb{E} [H_{loc}^2] - \mathbb{E}^2 [H_{loc}], \\ H_{loc} &= \frac{\langle x|\hat{H}|\Psi_\theta\rangle}{\langle x|\Psi_\theta\rangle}. \end{aligned} \quad (3)$$

However, $\text{Var}[E]$ depends on the system size and the overall energy scale of the Hamiltonian, which is an indirect measure of the true energy difference. To address this problem, here we adopt the so-called V-score [64]:

$$V = \frac{N\text{Var}[E]}{(E - E_T)^2}, \quad (4)$$

which is a more robust, dimensionless, and size-independent metric of variational accuracy. Here N is the number of sites, and the denominator provides a normalising energy scale, where E is the variational energy and E_T is a fixed reference energy.

We obtain this reference energy by averaging the energies $\langle \Psi_\epsilon | \hat{H} | \Psi_\epsilon \rangle$ of several randomly-generated Slater determinants, $|\Psi_\epsilon\rangle$, each of which can be evaluated analytically using the Hartree-Fock formula at a negligible computational cost. This method avoids the explicit Monte Carlo sampling used in [64] when treating $|\Psi_\epsilon\rangle$ as a true random many-body state.

The second major source of error is the statistical uncertainty from the Monte Carlo sampling performed during both the NQS optimisation and properties sampling steps (see Fig. 2(a)). The numerical expectation of the observable from the Monte Carlo sampling is distributed as a Gaussian variable, whose standard deviation scales inversely as the square root of the sample size M [56], i.e. $\sigma \sim O(1/\sqrt{M})$. This brings two critical uncertainties in the NQS solver:

1. Firstly, when using the V-score as the wave function optimisation metric, it carries intrinsic statistical uncertainty due to finite sampling. This uncertainty is addressed by applying a confidence interval correction proportional to $O(1/\sqrt{M})$ to the computed V-score; we denote the arrived metric score as **E-tol**.
2. Secondly, when sampling embedded physical properties from the optimised wave function, it introduces direct uncertainty into the quantum embedding loop. This uncertainty must be independently controlled, adhering strictly to the convergence criteria of the outer embedding iterations (see big blue arrows in Fig.1). To bound this error, we apply a stringent criterion, typically 3σ , corresponding to three times the standard deviation of the sampling expectation. This metric should be set lower than the convergence requirements of the embedding method. We denote the arrived properties sampling error metric as **P-tol**.

Notably, this convergence of P-tol often dominates the computational cost. For example, to reach a 0.001 residual for the embedding algorithm, it requires the error bound 3σ to be smaller than 5×10^{-4} , corresponding to a standard deviation of approximately $\sigma = 1.7 \times 10^{-4}$. This precision necessitates sampling in the order of 10^8 configurations (as $M \propto 1/\sigma^2$), often exceeding the computational resources required for the wave function optimisation itself.

By integrating the P-tol and E-tol metrics, we systematically control both the wave function optimisation and sampling errors. This guarantees the convergence stability of the NQS impurity solver. We will demonstrate the practical effectiveness of this combined error-control strategy in Section 3 below.

C. The gGA Algorithmic Structure

The gGA theoretical framework is rooted in the variational principle and, similarly to DMFT [7–12], in the

idea of the infinite-dimension limit [65]. Specifically, it is based on a variational wavefunction represented as $|\Psi_G\rangle = \hat{P}_G |\Psi_0\rangle$, where \hat{P}_G is an operator acting on a reference single-particle wavefunction (Slater determinant) $|\Psi_0\rangle$. The wavefunction $|\Psi_0\rangle$ is defined in an auxiliary Hilbert space, where the number of fermionic modes is the product of the number of physical Hilbert space's fermionic modes and a tunable factor B . This factor B governs the size of the variational space and the accuracy of the method. The operator \hat{P}_G maps states from the auxiliary space into the physical space, modifying the weights of the local electronic configurations of all fragments i . Both $|\Psi_0\rangle$ and \hat{P}_G are optimised to minimise the variational energy, evaluated neglecting all contributions that vanish in the limit of infinite-dimensional systems (as in DMFT). Therefore, like DMFT, the ghost-GA can accurately capture dynamical correlations, but not spatial correlations.

Here, we provide a brief overview of its algorithmic structure, with further technical details summarised in the appendix. We refer interested readers to the original papers cited above. For simplicity, we specialise the presentation focusing on the single-orbital Anderson lattice model:

$$\begin{aligned} \hat{H} = & \sum_{\langle i,j \rangle} \sum_{\sigma} (t_{ij} + \delta_{ij} \epsilon_p) \hat{p}_{i\sigma}^\dagger \hat{p}_{j\sigma} + \sum_i \hat{H}_{\text{loc}}^i [d_{i\sigma}, d_{i\sigma}^\dagger] \\ & + V \sum_{i\sigma} \left(\hat{p}_{i\sigma}^\dagger \hat{d}_{i\sigma} + \text{H.c.} \right) + \mu \sum_i \hat{N}_i, \end{aligned} \quad (5)$$

where:

$$\hat{H}_{\text{loc}}^i [d_{i\sigma}, d_{i\sigma}^\dagger] = \frac{U}{2} (\hat{n}_{di} - 1)^2. \quad (6)$$

Here the Fermionic operators $\{\hat{p}_{i\sigma}^\dagger, \hat{p}_{i\sigma}\}$ represent the uncorrelated degrees of freedom, while $\{\hat{d}_{i\sigma}^\dagger, \hat{d}_{i\sigma}\}$ represent the interacting orbitals; i, j are site labels, σ is the spin, μ is the chemical potential, and $\langle i, j \rangle$ indicating a sum over the first nearest neighbours. $\hat{n}_{di} = \sum_{\sigma} \hat{d}_{i\sigma}^\dagger \hat{d}_{i\sigma}$, $\hat{n}_{pi} = \sum_{\sigma} \hat{p}_{i\sigma}^\dagger \hat{p}_{i\sigma}$ and $\hat{N}_i = \hat{n}_{di} + \hat{n}_{pi}$. We focus on the paramagnetic phase and adopt uniform hopping terms t_{ij} , resulting in a semi-circular density of states characteristic of the infinite Bethe lattice, with energy measured in units of the half-bandwidth, consistent with previous studies [65].

The algorithmic structure of gGA, resulting from a convenient reformulation of the energy minimisation problem for the multiconfigurational wavefunction $|\Psi_G\rangle$ [20, 21, 28], closely mirrors that of DMFT, featuring a self-consistent iterative procedure nested within the solution of an embedding Hamiltonian (EH), which

serves as the impurity model:

$$\begin{aligned} \hat{H}^{\text{emb}}[\mathcal{D}, \Lambda^c] &= \sum_{a=1}^B \sum_{\sigma=\uparrow\downarrow} \left([\mathcal{D}_i]_a d_{i\sigma}^\dagger b_{ia\sigma} + \text{H.c.} \right) \\ &+ \sum_{a,b=1}^B \sum_{\sigma=\uparrow\downarrow} [\Lambda_i^c]_{ab} b_{ib\sigma} b_{ia\sigma}^\dagger \\ &+ \sum_{\sigma=\uparrow\downarrow} \hat{H}_{\text{loc}}^i \left[d_{i\sigma}, d_{i\sigma}^\dagger \right]. \end{aligned} \quad (7)$$

The variational optimisation of the parameters \mathcal{D}_i and Λ_i^c ensure that the feedback between local electronic correlations and the global electron density is consistently accounted for, describing how each atomic fragment interacts with its environment.

Once convergence is achieved, observables such as the ground-state total energy of Eq. (5) and the spectral function can be explicitly computed from the optimised variational parameters.

The ghost-GA algorithmic structure outlined above has two key computational advantages: (I) In gGA, it is sufficient to solve an EH with a relatively small bath ($B = 3$) to obtain the level of accuracy that DMFT achieves with infinite bath degrees of freedom. (II) While in DMFT it is necessary to compute local Green's function of the fragment i , the ghost-GA requires only the iterative calculation of the entries of the following ground-state single-particle density-matrix entries of the EH: $\langle \Phi | b_{ia\sigma}^\dagger b_{ib\sigma} | \Phi \rangle$ and $\langle \Phi | d_{i\sigma}^\dagger b_{ib\sigma} | \Phi \rangle$.

However, solving the EH remains the primary computational bottleneck. In the following section, we benchmark our proposed neural quantum state framework against exact diagonalisation, demonstrating its accuracy and supporting its feasibility in future gGA applications to multi-orbital materials, such as f-electron systems.

3. Benchmark Calculations of the ALM

In this Section we present gGA benchmark calculations on the single-orbital ALM on a Bethe lattice, see Eq. (5), within the limit of infinite coordination number, with a semicircular free density of states:

$$\rho(\epsilon) = \frac{2\sqrt{D^2 - \epsilon^2}}{\pi D^2}. \quad (8)$$

From now on we set the half-bandwidth D as the energy unit.

We evaluate the performance of our NQS-based impurity solver, which exhibits a rich interplay between Mott physics and the hybridisation between correlated and itinerant degrees of freedom, controlled by the on-site energy shift ϵ_p and the Hubbard interaction U .

To benchmark the accuracy of our NQS solver, we fixed $\epsilon_p = -1$ and considered two representative values of U :

$U = 0.5$ (metallic phase) and $U = 3$ (Mott insulating phase), assessing the performance of our method in both regimes.

Our results are shown in Fig. 3 and Table. I. In Fig. 3 is shown the gGA spectral function, see Eq. (9):

$$\mathcal{A}(\epsilon, \omega) = -\frac{1}{\pi} \text{ImTr} [\mathcal{G}(\epsilon, \omega)], \quad (9)$$

and the corresponding density of states:

$$A(\omega) = \int d\epsilon \rho(\epsilon) \mathcal{A}(\epsilon, \omega). \quad (10)$$

The Green's functions are computed from the non-interacting Hamiltonian. At $U = 0.5$, the spectral function clearly shows metallic behaviour with finite density at the Fermi level. On the other hand, at $U = 3.0$, a gap appears, characteristic of a Mott insulator. By comparing results using an ED solver, it is confirmed that our NQS solver accurately captures the qualitative differences between these phases of the model.

Quantitative occupation number results are presented in Table. I. Both impurity (d) and bath (p) orbitals exhibit fractional occupations consistent with metallic behaviour, showing minimal numerical differences (around 10^{-3}), compared to ED. While in the insulating phase ($U = 3$), the strong correlation fixes the electron in the p orbital, making it almost fully filled. We observe that both ED and NQS methods have an almost fully occupied p orbital, which explains the insulating gap in the spectrum function. The NQS solver shows slightly larger numerical differences in the impurity orbital occupancy in the insulating phase (as compared to ED), primarily due to stringent numerical accuracy requirements imposed by the gGA algorithm in strongly correlated regimes.

TABLE I. The orbital occupation number computed at $U = 0.5$ and $U = 3.0$ by exact diagonalisation (ED) and neural quantum state (NQS) solver.

Method	$U = 0.5$		$U = 3.0$	
	\mathbf{n}_d	\mathbf{n}_p	\mathbf{n}_d	\mathbf{n}_p
NQS	0.66579	0.8353	0.6579	0.9242
ED	0.66359	0.8348	0.5589	0.9348

Overall, our results showcase the effectiveness and suitability of the NQS solver within the gGA quantum embedding framework. Specifically, for gGA, the favourable computational scaling properties of NQS suggest potential for extending calculations to impurity models with larger orbital counts, potentially paving the way for applications to multi-orbital complex strongly correlated material systems beyond the reach of other methods.

A. Error control analysis.

In this section, we present the error control metric E-tol and P-tol by comparing the convergence and time

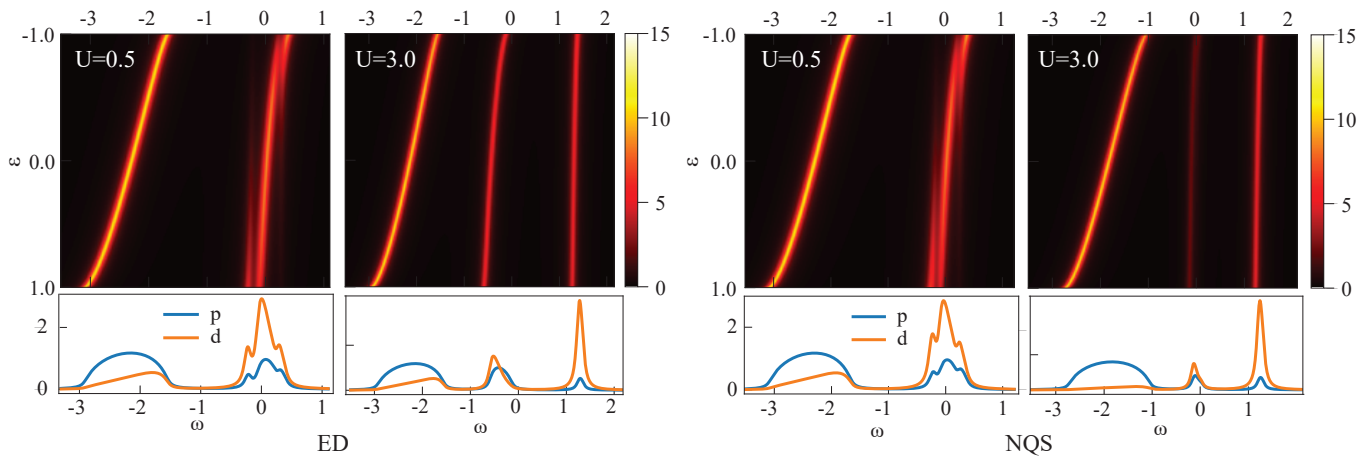


FIG. 3. The comparison of the solution of the Anderson lattice model using ED and NQS, combining with the gGA quantum embedding method. The band spectrum and density of states (DOS) are displayed. The convergence criteria are $1e-3$ for both methods. The NQS impurity solver reproduces the phase difference correctly.

cost during independent ghost-gutzwiller quantum embedding loops using the NQS impurity solver. In this analysis, we adopted $U = 0.5$ metal phase Anderson lattice model discussed in the last section as a running example. We set the bounds for error control metrics P-tol and E-tol as ϵ_p and ϵ_t , which are chosen among $(10^{-3}, 5 \times 10^{-4}, 10^{-4})$. All other settings, including the network structure, sizes, and the VMC optimisation parameters, are kept consistent in all tests. The analysis results are displayed in Fig. 4. From this, we verified the joint importance of both E-tol and P-tol. We also observe considerable growth of the time cost when reducing the bound ϵ_p for P-tol.

First, we display the residual computed from the maximum absolute difference of the gGA parameters \mathcal{R}_i and Λ_i between the previous and current iterations. The results are arranged in subfigures (a)-(c) of Fig. 4. In all cases, the residual decays rapidly in the first several iterations, followed by long and slow convergence to smaller values. The decrease of ϵ_t can assist in reducing the residual: for instance, for $\epsilon_t=10^{-4}$ (dark red line), lower residual results, compared to other cases when fixing the ϵ_p . Since this generally appears, we therefore conclude that the E-tol, which represents the wave function optimisation error, is important to the stability of the NQS VMC impurity solver. Moreover, comparing the three subfigures, we notice that the residual cannot be further reduced when ϵ_p is larger than 10^{-4} , regardless of the choice of the bound for E-tol. For instance, in Fig. 4(a) with $\epsilon_p = 10^{-3}$, it appears that all samples cannot converge to a considerably smaller residual. This is caused by the instabilities of sampled properties, which lead to unstable quantum-embedding loops. While for $\epsilon_p=10^{-4}$ (blue lines in Fig. 4 (c)), the convergence of all three samples with different ϵ_t is improved. This shows the importance of controlling the property sampling accuracy P-tol, in our method.

Nevertheless, a higher accuracy of the properties

(smaller P-tol) comes with considerable computational cost. In Fig. 4 (d), we displayed the time cost analysis of the properties sampling. We keep the colour convention consistent with (a)-(c), where lighter ones indicate higher ϵ_t and darker ones indicate smaller ϵ_t . We can clearly see the growth of the sampling time with the decrease of the bound of P-tol. We observe the time cost increases by over 100 times from $\epsilon_p=10^{-3}$ to 10^{-4} , while the increase is around 10 times to $\epsilon_t=5 \times 10^{-4}$. This aligns with the scaling of the VMC uncertainties ϵ , where $\epsilon \propto O(1/\sqrt{M})$. In this case, a decreased error tolerance ϵ by an order of magnitude would increase M by about 100 times. Comparably, the time cost for the wave function optimisation appears negligible, which only takes (1.63, 2.31, 5.70) seconds on average for ϵ_t among $(10^{-3}, 5 \times 10^{-4}, 10^{-4})$. From this, we also observe that the growth of computational time with the decrease of the bound of E-tol is rather gentle, compared with that of the parameter P-tol.

To conclude, the error analysis demonstrates that E-tol and P-tol are both important metrics for a numerically accurate solution. The dominant computational time cost is the properties sampling rather than the wave function optimisation. This finding calls for a better VMC sampling method to be innovated for quickly extracting the accurate physical observables from the NQS.

4. Discussion and summary

Employing NQS as an impurity solver offers several advantages. Due to the universal approximation capability of neural networks, accurately approximating the ground state wave function is feasible with properly designed network architectures, significantly reducing approximation errors common in other solvers. Furthermore, the favourable computational scaling properties of variational Monte Carlo (VMC) enable straightforward

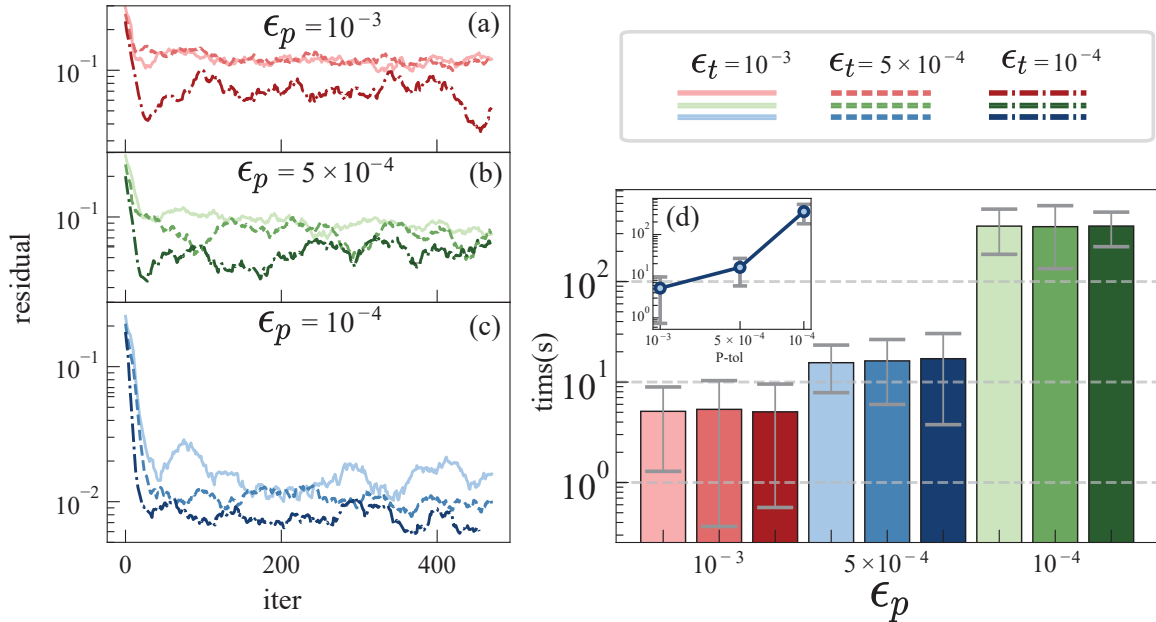


FIG. 4. The computational time cost and error analysis. (a)-(c): The residual during each self-consistent iteration of embedding loops using different error control parameters. (d) The time cost statistics during property sampling with different sampling accuracy.

extensions to multi-orbital models relevant for both theoretical investigation and realistic material simulation. Typically, the neural network evaluation scales as $O(N^2)$, while the Monte Carlo sampling scales as $O(N)$. With proper parallelisation on modern computers, such scalability suggests significant potential for studying complex systems such as strongly interacting f-orbital materials and the extended active-space models. This provides valuable possibilities for advancing research on strongly correlated electron systems.

Our study indicates that two remaining challenges need to be solved for further developing the most robust and general-purpose NQS impurity solver.

- **Accelerated computation of embedding properties.** Iterative updates in quantum embedding algorithms require precise computation of various physical observables. For example, the DMFT requires the Green's Function as the matching target, while the DMET and the gGA rely on accurate evaluation of single-body and/or two-body reduced density matrices. In practice, the sampling accuracy of these properties strongly affects the convergence of the entire embedding algorithm. Insufficient sampling accuracy can result in violations of fundamental physical constraints, therefore potentially destabilising the iterative embedding cycle, as found in our analysis. Given the slow $O(1/\sqrt{M})$ convergence of the sampling accuracy, a naive sampling strategy requires very large computational resources - for instance, roughly 10^8 samples to reach an accuracy of 10^{-3} . Therefore, developing

an enhanced or importance sampling method tailored specifically to NQS-VMC represents a useful research direction for enhancing computational efficiency and broadening the applicability of the NQS method.

- **Incorporating spin Symmetries in NQS wave function.** In strongly correlated electronic systems, it is often necessary to enforce specific spin symmetries (e.g., spin degeneracy, collinear, non-collinear spin configurations, etc). However, embedding these symmetries explicitly into NQS wave functions is nontrivial. Incorrect symmetries could lead to convergence issues and a physically incorrect solution. One practice, employed in this study, involves manually symmetrising computed properties post hoc. This approach, however, may introduce potential instability and convergence risk. Developing neural network architectures capable of inherently encoding spin symmetry should enhance the numerical stability and physical reliability of NQS impurity solvers.

In summary, we have designed and benchmarked an NQS-based impurity solver with an error control system. When integrated with the ghost Gutzwiller Approximation on the Anderson Lattice Model, our solver accurately captures the key electronic properties of both its metallic and Mott insulating phases, yielding results in excellent agreement with exact diagonalisation. Importantly, our analysis of the computational budget identifies the primary bottleneck not as the wave function optimisation, but as the high-accuracy property sampling

required by the embedding loop. This finding, therefore, establishes the development of efficient, high-precision sampling methods as the primary challenge to establishing NQS as a practical impurity solver within quantum embedding methods.

Code and data availability

The full data and the code to reproduce the results of this work are publicly available on the GitHub website. The website link is: (<https://github.com/floatingCatty/Hubbard>). For the ED solver, we employ the QuSpin packages (<https://quspin.github.io/QuSpin/>). The NQS is writ-

ten as an extension to the advanced VMC package quantax (<https://github.com/ChenAo-Phys/quantax>).

Acknowledgments

We gratefully acknowledge the financial support of the Natural Science and Engineering Research Council of Canada (Z.Z. and H.G.). T.-H.L. gratefully acknowledges funding from the National Science and Technology Council (NSTC) of Taiwan under Grant No. NSTC 112-2112-M-194-007-MY3. N.L. acknowledges support from the National Science Foundation under Award No. DMR-2532771. We thank the Digital Research Alliance Canada for providing substantial computational facilities, which made this work possible.

-
- [1] G. D. Mahan, *Many-particle physics* (Springer Science & Business Media, 2013).
- [2] R. Adler, C.-J. Kang, C.-H. Yee, and G. Kotliar, Correlated materials design: prospects and challenges, *Reports on Progress in Physics* **82**, 012504 (2018).
- [3] Q. Sun and G. K.-L. Chan, Quantum embedding theories, *Accounts of chemical research* **49**, 2705 (2016).
- [4] H. Ma, N. Sheng, M. Govoni, and G. Galli, Quantum embedding theory for strongly correlated states in materials, *Journal of Chemical Theory and Computation* **17**, 2116 (2021).
- [5] G. Knizia and G. K.-L. Chan, Density matrix embedding: A strong-coupling quantum embedding theory, *Journal of chemical theory and computation* **9**, 1428 (2013).
- [6] C. Mejuto-Zaera and M. Fabrizio, Efficient computational screening of strongly correlated materials: Multiorbital phenomenology within the ghost gutzwiller approximation, *Physical Review B* **107**, 235150 (2023).
- [7] V. Anisimov and Y. Izyumov, *Electronic Structure of Strongly Correlated Materials* (Springer, 2010).
- [8] V. I. Anisimov, A. I. Oteryaev, M. A. Korotin, A. O. Anokhin, and G. Kotliar, First-principles calculations of the electronic structure and spectra of strongly correlated systems: dynamical mean-field theory, *J. Phys. Condens. Matter* **9**, 7359 (1997).
- [9] K. Held, A. Nekrasov, G. Keller, V. Eyert, N. Blümer, A. K. McMahan, R. T. Scalettar, T. Pruschke, V. I. Anisimov, and D. Vollhardt, Realistic investigations of correlated electron systems with LDA+DMFT, *Phys. Stat. Sol. (B)* **243**, 2599 (2006).
- [10] A. Georges, G. Kotliar, W. Krauth, and M. J. Rozenberg, Dynamical mean-field theory of strongly correlated fermion systems and the limit of infinite dimensions, *Reviews of modern physics* **68**, 13 (1996).
- [11] J.-Z. Zhao, J.-N. Zhuang, X.-Y. Deng, Y. Bi, L.-C. Cai, Z. Fang, and X. Dai, Implementation of LDA+DMFT with the pseudo-potential-plane-wave method, *Chin. Phys. B* **21**, 057106 (2012).
- [12] G. Kotliar, S. Y. Savrasov, K. Haule, V. S. Oudovenko, O. Parcollet, and C. Marianetti, Electronic structure calculations with dynamical mean-field theory, *Reviews of Modern Physics* **78**, 865 (2006).
- [13] S. Y. Savrasov, G. Kotliar, and E. Abrahams, Correlated electrons in δ -plutonium within a dynamical mean-field picture, *Nature* **410**, 793 (2001).
- [14] A. Paul and T. Birol, Applications of dft+ dmft in materials science, *Annual Review of Materials Research* **49**, 31 (2019).
- [15] G. Knizia and G. K.-L. Chan, Density matrix embedding: A simple alternative to dynamical mean-field theory, *Physical review letters* **109**, 186404 (2012).
- [16] M. R. Hermes, R. Pandharkar, and L. Gagliardi, Variational localized active space self-consistent field method, *Journal of Chemical Theory and Computation* **16**, 4923 (2020).
- [17] S. Wouters, C. A. Jiménez-Hoyos, Q. Sun, and G. K.-L. Chan, A practical guide to density matrix embedding theory in quantum chemistry, *Journal of chemical theory and computation* **12**, 2706 (2016).
- [18] S. Sekaran, M. Tsuchiizu, M. Saubanère, and E. Fromager, Householder-transformed density matrix functional embedding theory, *Physical Review B* **104**, 035121 (2021).
- [19] Z.-H. Cui, T. Zhu, and G. K.-L. Chan, Efficient implementation of ab initio quantum embedding in periodic systems: Density matrix embedding theory, *Journal of Chemical Theory and Computation* **16**, 119 (2019).
- [20] N. Lanatà, T.-H. Lee, Y.-X. Yao, and V. Dobrosavljević, Emergent bloch excitations in mott matter, *Physical Review B* **96**, 195126 (2017).
- [21] M. S. Frank, T.-H. Lee, G. Bhattacharyya, P. K. H. Tsang, V. L. Quito, V. Dobrosavljević, O. Christiansen, and N. Lanatà, Quantum embedding description of the anderson lattice model with the ghost gutzwiller approximation, *Physical Review B* **104**, L081103 (2021).
- [22] T.-H. Lee, C. Melnick, R. Adler, X. Sun, Y. Yao, N. Lanatà, and G. Kotliar, Charge self-consistent density functional theory plus ghost rotationally invariant slave-boson theory for correlated materials, *Physical Review B* **110**, 115126 (2024).
- [23] N. Lanatà, Derivation of the ghost gutzwiller approximation from quantum embedding principles: Ghost density matrix embedding theory, *Physical Review B* **108**, 235112 (2023).

- [24] N. Lanatà, Operatorial formulation of the ghost rotationally invariant slave-boson theory, *Physical Review B* **105**, 045111 (2022).
- [25] T.-H. Lee, N. Lanatà, and G. Kotliar, Accuracy of ghost rotationally invariant slave-boson and dynamical mean field theory as a function of the impurity-model bath size, *Physical Review B* **107**, L121104 (2023).
- [26] T.-H. Lee, C. Melnick, R. Adler, N. Lanatà, and G. Kotliar, Accuracy of ghost-rotationally-invariant slave-boson theory for multiorbital hubbard models and realistic materials, *Physical Review B* **108**, 245147 (2023).
- [27] M. C. Gutzwiller, Correlation of Electrons in a Narrow s Band, *Phys. Rev.* **137**, A1726 (1965).
- [28] N. Lanatà, Y. X. Yao, C.-Z. Wang, K.-M. Ho, and G. Kotliar, Phase diagram and electronic structure of praseodymium and plutonium, *Phys. Rev. X* **5**, 011008 (2015).
- [29] N. Lanatà, P. Barone, and M. Fabrizio, Fermi-surface evolution across the magnetic phase transition in the Kondo lattice model, *Phys. Rev. B* **78**, 155127 (2008).
- [30] X.-Y. Deng, L. Wang, X. Dai, and Z. Fang, Local density approximation combined with Gutzwiller method for correlated electron systems: Formalism and applications, *Phys. Rev. B* **79**, 075114 (2009).
- [31] K. M. Ho, J. Schmalian, and C. Z. Wang, Gutzwiller density functional theory for correlated electron systems, *Phys. Rev. B* **77**, 073101 (2008).
- [32] N. Lanatà, H. U. R. Strand, X. Dai, and B. Hellsing, Efficient implementation of the Gutzwiller variational method, *Phys. Rev. B* **85**, 035133 (2012).
- [33] J. Bünemann, F. Gebhard, T. Ohm, S. Weiser, and W. Weber, Gutzwiller-correlated wave functions: application to ferromagnetic nickel, in *Frontiers in Magnetic Materials*, edited by A. Narlikar (Springer, Berlin, 2005) p. 117.
- [34] C. Attacalite and M. Fabrizio, Properties of Gutzwiller wave functions for multiband models, *Phys. Rev. B* **68**, 155117 (2003).
- [35] D. Guerci, M. Capone, and N. Lanatà, Time-dependent ghost gutzwiller nonequilibrium dynamics, *Physical Review Research* **5**, L032023 (2023).
- [36] S. Giuli, C. Mejuto-Zaera, and M. Capone, Altermagnetism from interaction-driven itinerant magnetism, *Physical Review B* **111**, L020401 (2025).
- [37] M. Caffarel and W. Krauth, Exact diagonalization approach to correlated fermions in infinite dimensions: Mott transition and superconductivity, *Physical review letters* **72**, 1545 (1994).
- [38] M. Capone, L. de’Medici, and A. Georges, Solving the dynamical mean-field theory at very low temperatures using the lanczos exact diagonalization, *Physical Review B—Condensed Matter and Materials Physics* **76**, 245116 (2007).
- [39] K. G. Wilson, The renormalization group: Critical phenomena and the kondo problem, *Reviews of modern physics* **47**, 773 (1975).
- [40] R. Bulla, T. A. Costi, and T. Pruschke, Numerical renormalization group method for quantum impurity systems, *Reviews of Modern Physics* **80**, 395 (2008).
- [41] S. R. White, Density matrix formulation for quantum renormalization groups, *Physical review letters* **69**, 2863 (1992).
- [42] U. Schollwöck, The density-matrix renormalization group, *Reviews of modern physics* **77**, 259 (2005).
- [43] E. Gull, A. J. Millis, A. I. Lichtenstein, A. N. Rubtsov, M. Troyer, and P. Werner, Continuous-time monte carlo methods for quantum impurity models, *Reviews of Modern Physics* **83**, 349 (2011).
- [44] A. N. Rubtsov, V. V. Savkin, and A. I. Lichtenstein, Continuous-time quantum monte carlo method for fermions, *Physical Review B—Condensed Matter and Materials Physics* **72**, 035122 (2005).
- [45] G. Carleo and M. Troyer, Solving the quantum many-body problem with artificial neural networks, *Science* **355**, 602 (2017).
- [46] O. Sharir, A. Shashua, and G. Carleo, Neural tensor contractions and the expressive power of deep neural quantum states, *Physical Review B* **106**, 205136 (2022).
- [47] A. Chen and M. Heyl, Empowering deep neural quantum states through efficient optimization, *Nature Physics* **20**, 1476 (2024).
- [48] J. R. Moreno, G. Carleo, A. Georges, and J. Stokes, Fermionic wave functions from neural-network constrained hidden states, *Proceedings of the National Academy of Sciences* **119**, e2122059119 (2022), <https://www.pnas.org/doi/pdf/10.1073/pnas.2122059119>.
- [49] G. Goldshlager, N. Abrahamson, and L. Lin, A kaczmarz-inspired approach to accelerate the optimization of neural network wavefunctions, *Journal of Computational Physics* **516**, 113351 (2024).
- [50] Y. Levine, O. Sharir, N. Cohen, and A. Shashua, Quantum entanglement in deep learning architectures, *Physical review letters* **122**, 065301 (2019).
- [51] H. Lange, A. Van de Walle, A. Abedinnia, and A. Bohrdt, From architectures to applications: A review of neural quantum states, *Quantum Science and Technology* (2024).
- [52] H. Yokoyama and H. Shiba, Variational monte-carlo studies of hubbard model. i, *Journal of the Physical Society of Japan* **56**, 1490 (1987).
- [53] H. Ma, H. Shang, and J. Yang, Quantum embedding method with transformer neural network quantum states for strongly correlated materials, *npj Computational Materials* **10**, 220 (2024).
- [54] X. Cao, Z. Zhong, and Y. Lu, Vision transformer neural quantum states for impurity models, *arXiv preprint arXiv:2408.13050* (2024).
- [55] A. Chen, Z.-Q. Wan, A. Sengupta, A. Georges, and C. Roth, Neural network-augmented pfaffian wavefunctions for scalable simulations of interacting fermions, *arXiv preprint arXiv:2507.10705* (2025).
- [56] F. Becca and S. Sorella, *Quantum Monte Carlo approaches for correlated systems* (Cambridge University Press, 2017).
- [57] S. Brooks, Markov chain monte carlo method and its application, *Journal of the royal statistical society: series D (the Statistician)* **47**, 69 (1998).
- [58] S. Sorella, Green function monte carlo with stochastic reconfiguration, *Physical review letters* **80**, 4558 (1998).
- [59] Y. Lu, M. Höppner, O. Gunnarsson, and M. Haverkort, Efficient real-frequency solver for dynamical mean-field theory, *Physical Review B* **90**, 085102 (2014).
- [60] Y. Lu, X. Cao, P. Hansmann, and M. Haverkort, Natural-orbital impurity solver and projection approach for green’s functions, *Physical Review B* **100**, 115134 (2019).

- [61] H. Shang, C. Guo, Y. Wu, Z. Li, and J. Yang, Solving schrödinger equation with a language model, arXiv preprint arXiv:2307.09343 (2023).
- [62] A. Vaswani, N. Shazeer, N. Parmar, J. Uszkoreit, L. Jones, A. N. Gomez, L. Kaiser, and I. Polosukhin, Attention is all you need, *Advances in neural information processing systems* **30** (2017).
- [63] S. Brody, U. Alon, and E. Yahav, How attentive are graph attention networks?, arXiv preprint arXiv:2105.14491 (2021).
- [64] D. Wu, R. Rossi, F. Vicentini, N. Astrakhantsev, F. Becca, X. Cao, J. Carrasquilla, F. Ferrari, A. Georges, M. Hibat-Allah, *et al.*, Variational benchmarks for quantum many-body problems, *Science* **386**, 296 (2024).
- [65] W. Metzner and D. Vollhardt, Correlated lattice fermions in infinite dimensions, *Physical review letters* **62**, 324 (1989).

1. Evaluation of the reference mean-field energy E_T .

As discussed in the main text, we choose the E_T in the V-score computation:

$$V = \frac{N\text{Var}[E]}{(E - E_T)^2}, \quad (\text{A1})$$

as the energy expectation of a random mean-field wave function. Therefore, we can use the closed-form Hartree-

Fock formula to estimate the energy accurately, reducing the need for sampling.

To construct the random mean-field solution with the physical constraint, we used a parameterisation technique. The closed-form Hartree-Fock energy expression is:

$$E_{hf} = \frac{1}{2}\text{Tr}[D \cdot h] + \frac{1}{2}\text{Tr}[D \cdot F], \quad (\text{A2})$$

where the h are the one-body terms of the original system Hamiltonian, and the F is the corresponding Fock matrix.

Since this expression is related directly to the density matrix, we need to design a sampling method to ensure the density matrix respects the physical constraints, such as particle conservation and idempotency. To achieve this, we first generate a random hermitian matrix A , then, by performing the QR decomposition, we attain a set of orthogonal random basis vectors Q . Afterwards, by selecting n columns of matrix $Q^{(n)} = Q[0 : n]$ (n is the total electron occupation number), and multiplying by its conjugate transpose, we have the sampled form $\tilde{D} = Q^{(n)}Q^{(n)\dagger}$. The matrix \tilde{D} follows all the required properties of the physical mean-field density matrix. Later on, we use \tilde{D} to construct the Fock matrix F , therefore solving the energy using the above formula. The energy is computed and averaged by generating new \tilde{D} and F until a convergence criterion is reached.